PHYSICS

First demonstration of antimatter wave interferometry

S. Sala[1,2], A. Ariga[3], A. Ereditato[3], R. Ferragut[4,2]*, M. Giammarchi[2]*, M. Leone[4], C. Pistillo[3]*, P. Scampoli[3,5]

Interference of matter waves is at the heart of quantum physics and has been observed for a wide range of particles from electrons to complex molecules. Here, we demonstrate matter wave interference of single positrons using a period-magnifying Talbot-Lau interferometer based on material diffraction gratings. The system produced high-contrast periodic fringes, which were detected by means of nuclear emulsions capable of determining the impact point of each individual positron with submicrometric resolution. The measured energy dependence of fringe contrast in the range of 8 to 16 keV proves the quantum-mechanical origin of the periodic pattern and excludes classical projective effects, providing the first observation to date of antimatter wave interference. Future applications of this interferometric technique include the measurement of the gravitational acceleration of neutral antimatter systems exploiting the inertial sensing capabilities of Talbot-Lau interference.

INTRODUCTION

In 1923, de Broglie (*1*, *2*) introduced the concept of wave-particle duality: the Planck constant h relates the momentum p of a massive particle to its de Broglie wavelength $\lambda_{dB} = h/p$. The superposition principle is one of the main postulates of quantum mechanics; diffraction and interference phenomena are, therefore, predicted and have been observed on objects of increasing complexity, from electrons (*3*, *4*) to neutrons (*5*, *6*) and molecules (*7*–*9*). Beyond the early electron diffraction experiments (*3*, *4*), the demonstration of single-electron double-slit–like interference was a highly sought-after result. Initially proposed by Feynman as a thought experiment, it was last carried out in 1976 (*10*). A few years later, positron diffraction was first observed (*11*). However, an analog of the double-slit experiment has not been performed to date on any system containing antimatter. To bridge this gap, we designed and realized a Talbot-Lau interferometer (*12*) suited to a low-energy positron beam. This interferometric technique could also lead to studies of fundamental interest on neutral antimatter systems. For instance, several techniques are being considered to undertake the measurement of the gravitational acceleration of positronium, muonium, and antihydrogen (*13*–*20*). Talbot-Lau–based inertial sensing (*21*) offers the capability to work with low-intensity, weakly coherent beams similar to the one used in this work. This is a highly desirable feature for beam-based experiments with antimatter.

RESULTS

The experiment makes use of the variable energy positron beam facility of the L-NESS (Laboratory for Nanostructure Epitaxy and Spintronics on Silicon) in Como (Italy). Positrons (e^+) from the beta decay of a ^{22}Na radioactive source are implanted on a monocrystalline tungsten film and emitted with a kinetic energy of about 3 eV, determined by the work function of the material (*22*). Slow positrons are then accelerated up to 16 keV by means of a purely electrostatic system. A monochromatic and continuous beam is thus formed with an energy spread less than 0.1%, limited by the stability of the power supplies. The positron rate is $(5 \pm 1) \times 10^3$ e^+/s, and beam focusing can be tuned to reach a spot size of the order of several millimeters of full width at half maximum (FWHM), an approximately Gaussian intensity profile (*23*) and an angular divergence at the level of a few milliradians (*24*). A suitable model (*25*) of grating-based interferometry with a partially coherent beam exploits the analogy with Gaussian Schell-model beams of classical optics (Materials and Methods). Within this formalism, incoherence translates physically into a broad transverse momentum distribution and mathematically to a short transverse coherence length l. The L-NESS beam features a coherence length of the order of a few nanometers. An effective configuration for these conditions was obtained with a novel period-magnifying two-grating interferometer (*21*, *26*). It exploits an intermediate working regime between the standard Talbot-Lau setup, where the two gratings and the detector are equally spaced, and the so-called Lau interferometer (*27*), which has more stringent coherence requirements (*25*). By means of unequal grating periodicities, the system provides sizable period magnification in a relatively compact setup (*21*). In particular, we used gold-coated 700-nm-thick silicon nitride (SiN) gratings with periodicity $d_1 = (1.210 \pm 0.001)$ μm and $d_2 = (1.004 \pm 0.001)$ μm to produce a $d_3 = (5.90 \pm 0.04)$ μm periodic interference pattern. Both gratings have a nominal open fraction of 50%.

The periodic spatial distribution generated by the interferometer (Fig. 1) is revealed by a nuclear emulsion detector. Nuclear emulsions (*28*) offer submicrometer-level position resolution in the detection of ionizing particles (*24*, *29*). They work as photographic films by exploiting the properties of silver bromide crystals embedded in a 50-μm-thick gelatin matrix. For this experiment, we developed a glass-supported emulsion detector (fig. S1) and experimentally demonstrated its capability to resolve periodic patterns at the micrometric scale even with low signal contrast and on large areas (*24*).

Interferometer alignment is particularly challenging, and it is intimately connected to beam coherence. The Talbot-Lau interferometer can produce high-contrast fringes if the resonance condition (*21*)

$$\frac{L_1}{L_2} = \frac{d_1}{d_2} - 1 \qquad (1)$$

[1]Dipartimento di Fisica "Aldo Pontremoli," Università degli Studi di Milano, via Celoria 16, 20133 Milano, Italy. [2]Istituto Nazionale di Fisica Nucleare (INFN), Sezione di Milano, via Celoria 16, 20133 Milano, Italy. [3]Albert Einstein Center for Fundamental Physics, Laboratory for High Energy Physics, University of Bern, Sidlerstrasse 5, 3012 Bern, Switzerland. [4]L-NESS and Department of Physics, Politecnico di Milano, via Anzani 42, 22100 Como, Italy. [5]Dipartimento di Fisica "Ettore Pancini," Università di Napoli Federico II, Complesso Universitario di Monte S. Angelo, 80126 Napoli, Italy.
*Corresponding author. Email: rafael.ferragut@polimi.it (R.F.); marco.giammarchi@mi.infn.it (M.G); ciro.pistillo@lhep.unibe.ch (C.P.)

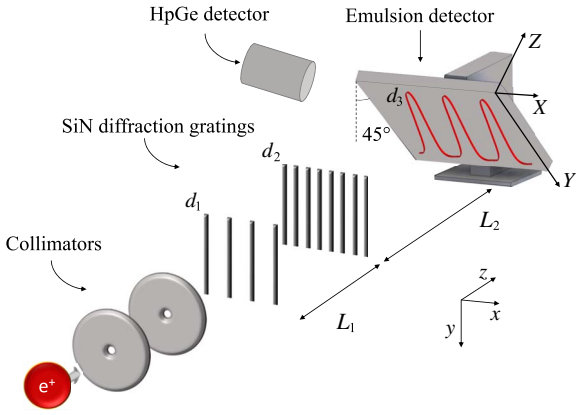

Fig. 1. Schematics of the Talbot-Lau interferometer. Positrons traverse two circular 2-mm-wide collimators 10.2 cm apart. The interferometer is composed of two SiN diffraction gratings with periodicity d_1 and d_2, respectively, separated by L_1 = (118.1 ± 0.2) mm. Interference fringes with d_3 periodicity are expected at L_2 = (576 ± 5) mm. The emulsion is tilted so that the *Y* axis in the reference frame of the emulsion surface (*X*, *Y*) forms a 45° angle with the *y* axis of the laboratory. Gamma rays (511 keV) from positron annihilation in the emulsion are monitored with a high-purity germanium (HpGe) detector for rate measurement.

is met, even for a fully incoherent ($l \to 0$) beam. However, as this regime is approached, the required accuracy at which the above condition should be ensured increases. To improve the tolerance to possible misalignments, we collimated the beam by means of two circular openings (Fig. 1). Regardless of beam coherence, the experimental uncertainty on the optimal (resonance) value of the ratio $\frac{L_1}{L_2}$ that stems from the errors on the measured grating periods amounts to $\sigma_{L_1/L_2} = 0.002$. In the adopted geometry, this corresponds to an uncertainty of 5 mm on the ideal detector location L_2. To circumvent this issue, we operated emulsion films tilted by 45° in such a way that the *Y* coordinate of the emulsion plane is correlated to L_2, which varies along the *z* axis in the laboratory reference frame (Fig. 1). We thus performed a position scan in a single exposure by analyzing different horizontal slices of the emulsion detector.

The relative rotational alignment of the two gratings is a critical parameter, as contrast follows a Gaussian modulation as a function of the ϕ angle formed by the slits, with standard deviation (*25*)

$$\sigma_\phi = \frac{1}{\sqrt{2\pi}} \frac{d_2 l^{\mathrm{det}}}{L_2 \lambda_{\mathrm{dB}}} \tag{2}$$

where l^{det} is the coherence length computed at the detector plane by an analytical model (Materials and Methods) (*25*). Throughout the measurements, the ratio $\frac{l^{\mathrm{det}}}{\lambda_{\mathrm{dB}}} \sim 800$ remained approximately constant, which yielded a tolerance $\sigma_\phi \sim 550$ μrad for the collimated beam. The second grating was mounted on a piezoelectric rotation stage with nominal resolution of 0.8 μrad; the adopted alignment protocol (Materials and Methods) ensures that $\phi < 70$ μrad for the full duration of the exposures. All the components of the interferometer, including the rotation stage, were nonmagnetic, and the interferometer was surrounded by a mu-metal shield designed to reduce residual Earth magnetic field to less than 0.5 μT. Parallelism between the interferometer optical axis and the beam propagation axis was controlled at the level of 1 mrad by means of alignment lasers. The apparatus operated at a vacuum pressure between 10^{-7} and 10^{-6} mbar during each measurement. We configured the interferometer for maximum contrast at E = 14 keV (λ_{dB} = 10.3 pm) by setting $L_1 = \frac{d_1 d_2}{\lambda_{\mathrm{dB}}}$ (*21*). Since this geometry satisfies the Talbot-Lau resonance conditions, single-slit diffraction from the first to second grating plane is not negligible (as it would instead occur for $\frac{L_1 \lambda_{\mathrm{dB}}}{d_1} \ll d_2$). Therefore, a quantum-mechanical description of the system is required, which predicts a peculiar contrast dependence on the positron energy. To ensure uniform working conditions throughout the explored energy range, we used nuclear emulsions prepared without the standard surface protective gelatin layer. The presence of even a micrometric layer would have introduced detection efficiency (*23*) and positron trajectory smearing (*24*) that are both energy dependent. Thermally induced grains are the dominant source of background noise in emulsion detectors. Nonetheless, no measurable increase in the average density of noise grains was observed for the unprotected emulsions compared to standard detectors used under the same conditions.

We now summarize the results of five beam exposures performed for the positron energies of 16, 14, 11, 9, and 8 keV. Since the transport efficiency through the collimated L-NESS electrostatic beam decreases rapidly below 8 keV, lower energies would have required unpractically long exposure times. On the other hand, energies higher than 16 keV would have run into power supply stability and vacuum discharge limitations. The residual beam rate at the detector after collimation (~80% loss) and the passage through the gratings (~90% loss) was about 100 e^+/s. Exposure times between 120 and 200 hours were required to accumulate sufficient statistics (about 2×10^7 grains in the analysis region). These time intervals were selected to match the total counts under the 511 keV annihilation peak on the calibrated HpGe detector (*23*) measured at 14 keV. Beam focusing was tuned to ensure that beam spot size, and hence the geometrical features of the beam such as angular divergence, did not appreciably vary with the energy. Spot sizes deviated by less than 10% from the average value of 6.5 mm FWHM on the detector plane. Silver bromide crystals activated by the passage of the positrons through the emulsion become visible with optical microscopes after chemical development; we then processed the emulsions at the microscope scanning facility of the University of Bern. For each given *X*-*Y* position, the microscope grabbed a series of images by shifting the focal plane in the direction normal to the emulsion surface (*Z*). Grain clusters were reconstructed (*30*) to assign *X*, *Y*, and *Z* coordinates to the positron impact point (see Fig. 2). The data were subdivided in 370 × 294 μm^2 wide regions, which we refer to as views.

Each view was independently analyzed to search for periodicity in the impact point distribution by maximizing the so-called Rayleigh test function (*31*)

$$R(\alpha, d_3) = \left| \frac{1}{n} \sum_{j=1}^{n} \exp\left(\frac{2\pi i X_j(\alpha)}{d_3} \right) \right| \tag{3}$$

with respect to the period d_3 and the angle α between the fringes and the microscope reference frame. We introduced $X_j(\alpha)$ as the *X* coordinate of the *j*th grain in the view rotated by α. The effectiveness of this period-finding approach was experimentally demonstrated for similar applications (*24*, *32*). Values of the parameters maximizing *R*, namely, (α^*, d_3^*), were searched in the range −0.05 rad < α < 0.05 rad and 5.7 μm < d_3 < 6.1 μm. If a consistent periodic signal spanned a large area, then a

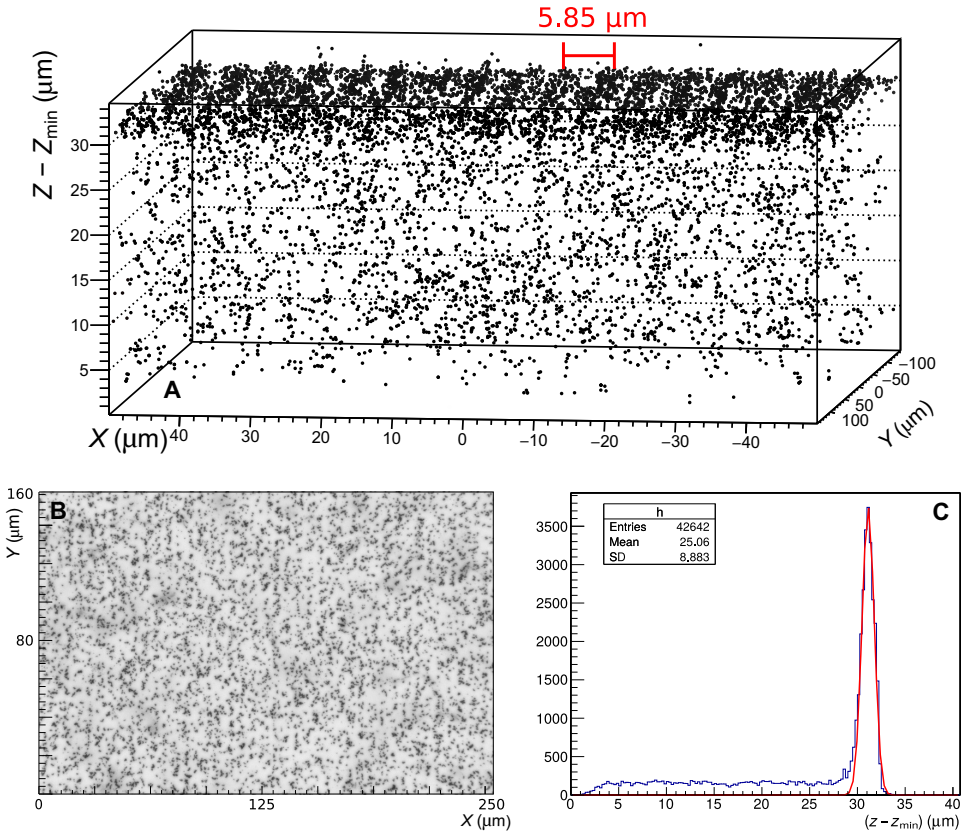

Fig. 2. Representative example of view analysis. All panels refer to the highest contrast view for E = 14 keV. (**A**) Three-dimensional distribution of the reconstructed clusters limited to a 100-μm-wide region along X. A hint of the periodic fringes is even appreciable by visual inspection. (**B**) Raw microscope image cropped to a region of 250 × 160 μm^2. (**C**) Histogram of the Z position of the clusters and Gaussian fit used to determine the analysis region.

distinctive peak would be expected in the (α^*, d_3^*) distribution over the analyzed views (*24*). A representative example is shown in Fig. 3 for the 14-keV exposure. A least-squares Gaussian fit to the data (Fig. 3) yields the detected period for each exposure, which is reported in Table 1. The statistical error (68% confidence interval) comes from the fit procedure, whereas the estimated 0.8% systematic error descends from the conversion between camera pixels and physical size (*24*). The measured period is compatible with the expected value d_3 = (5.90 ± 0.04) μm. Once the optimal period and angle were found, a histogram of $X_j(\alpha^*)$ mod d_3^* was constructed, where mod is the modulo operation on floating point numbers. The signal contrast was estimated by fitting the histogram with a d_3^*-periodic sinusoidal function appropriate for the phase structure of the fringes (Fig. 4A). We performed the subtraction of a constant background from the histogram by measuring the grain density in the bulk, as positrons can only penetrate a few micrometers of emulsion. This yielded an estimate of the number of grains due to the intrinsic emulsion noise entering the analysis region. This is limited to 340 × 270 μm^2 on the X-Y plane to remove areas affected by sizeable optical aberration. The depth in Z was determined with a Gaussian fit on the positron implantation profile (*24*). The average width of the selected region along the Z direction was 2.9 μm. We performed this procedure only for views contained in the 3σ elliptical region defined in Fig. 3. As the signal-to-noise ratio decreased moving away from the center of the beam spot, maximization of the Rayleigh test essentially converged to random values of (α^*, d_3^*) for views outside the elliptical region; contrast estimation for these views would give unphysical results. The contrast measured after noise subtraction is, in principle, independent from the signal-to-noise ratio. An average noise density ranging from 9 to 6 grains/1000 μm^3 was measured in the different exposures. The average number of grains per view entering

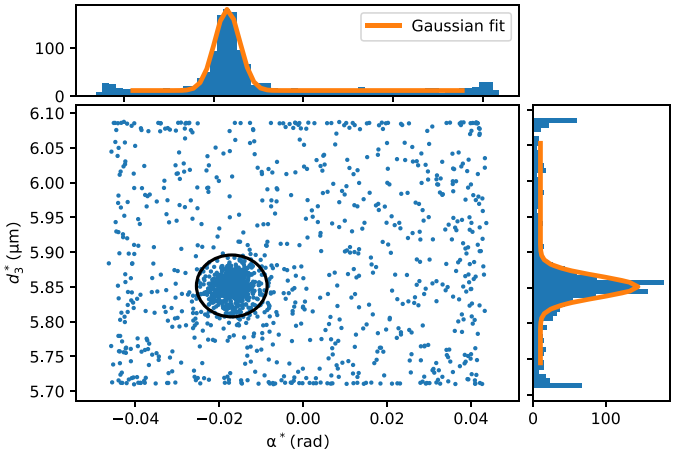

Fig. 3. Optimal angle and period found via the Rayleigh test. Scatter plot and profile histograms of the optimal period and angle $(\alpha^*, d_3^*)$for 14 keV. A total of 1620 views covering a surface of about 10 × 14 mm^2 were analyzed. Histograms are fit with a Gaussian function plus a constant background. The black ellipse indicates the corresponding 99.7% confidence level region. The corresponding plots for the other energy points are shown in fig. S2.

the analysis fluctuated within 10% from the mean value of 11,000. A two-dimensional heatmap of the measured contrast covering the scanned surface area is shown in Fig. 4B. Since Y is correlated to L_2, a contrast modulation was observed in the Y direction. The contrast dependence on X displayed a marked asymmetry, likely as a result of the limited beam coherence and alignment accuracy. We emphasize that this feature would have been hidden in a moving mask–based detection scheme. On the other hand, emulsions allowed direct fringe detection on a substantially larger area than the surface of the gratings (3×3 mm^2): The scanned area contained a sizable number ($\sim 10^4$) of consecutive high-visibility d_3-periodic fringes. Visual inspection of the two-dimensional maps already suggests that contrast is decreasing with the energy. To provide a quantitative estimate of the peak contrast, we selected views in a 1-mm-wide region (indicated by the dashed lines in Fig. 4B). The corresponding contrast for energies in the range of 8 to 14 keV encompassing the largest contrast modulation is shown in Fig. 4A as a function of the position of the geometrical center of the view. This is given in the reference frame of the center of the beam along the Y axis, which was estimated by means of a Gaussian fit to the intensity profile. The position of the beam is stable in the laboratory reference frame at the level of 0.5 mm. However, this reference frame is more robust with respect to manual positioning errors of the emulsion in the interferometer and in the microscope reference frame, both of which can be larger than 0.5 mm. The data were fit with a Gaussian function plus a constant background (Fig. 4A), which was used to estimate the maximum contrast for each energy. This is shown in Table 1, alongside the position of the contrast peak (Y_0) extracted from the same fit. Uncertainties on the contrast were computed from the fit parameters, whereas the error on Y_0 is dominated by the estimated stability of the beam and by the uncertainty in determining its center.

Table 1. Summary of the results at different energies. Measured fringe period d_3, contrast C, and peak contrast position Y_0, as discussed in the text.

E (keV)	d_3 (μm)	C (%)	Y_0 (mm)
16	$5.853 \pm 0.001_{stat} \pm 0.050_{syst}$	45.8 ± 1.5	−2.9 ± 0.6
14	$5.851 \pm 0.001_{stat} \pm 0.050_{syst}$	49.1 ± 0.5	−2.3 ± 0.6
11	$5.852 \pm 0.001_{stat} \pm 0.050_{syst}$	43.6 ± 0.8	−2.2 ± 0.6
9	$5.852 \pm 0.001_{stat} \pm 0.050_{syst}$	26.7 ± 0.8	−2.3 ± 0.6
8	$5.850 \pm 0.001_{stat} \pm 0.050_{syst}$	14.4 ± 0.8	−2.2 ± 0.6

DISCUSSION

We conclude that the peak contrast of the periodic signal was observed for different energies at the same distance $L_2 = (573 \pm 1)$ mm, where the uncertainty accounts for experimental errors in the absolute position of the center of the beam in the laboratory reference frame. The measured contrast modulation is in fair agreement with the expected behavior for a Talbot-Lau interferometer and is incompatible with classical moiré deflectometry (*33*), where particles propagate on ballistic trajectories through the gratings. Since this geometry could, in principle, produce

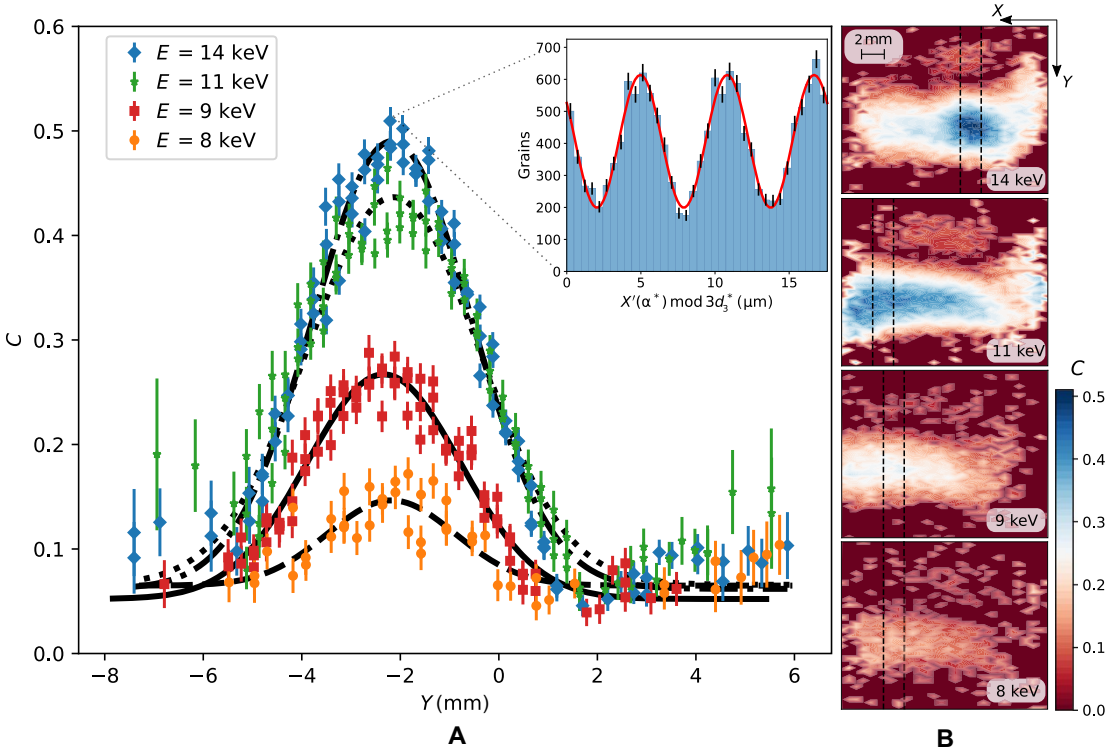

Fig. 4. Contrast on the emulsion surface. (**A**) Contrast C as a function of Y for views in the region delimited by the dashed lines in (B). The origin of the Y axis is set to coincide with the center of the beam intensity profile, estimated for each energy with a Gaussian fit. Errors on the contrast come from the sinusoidal least-squares fit. The result of a Gaussian fit with constant background is superimposed to the data. The inset shows a histogram of $X_j(\alpha^*)$ mod $3d^*$ and a sinusoidal fit for the highest contrast view; error bars represent Poissonian counting uncertainties. (**B**) Contrast heatmaps for the four energies considered. The contrast of views excluded from the analysis was set to zero.

a fringe pattern with the same periodicity from geometrical shadow effects alone (*21*), this conclusion holds only if spurious energy-dependent effects are ruled out. A possible source could be the energy-dependent positron transmission from the grating bars, which varies from about 0.1% at 8 keV to 49% at 14 keV. This contribution to background noise is, however, suppressed by a factor 10^4 with respect to the intrinsic emulsion noise due to the broad angular distribution of transmitted positrons (Materials and Methods). The measured contrast drop from the resonance value, defined as $C/C_{max}(E)$, is shown in Fig. 5 as a function of the energy and compared with the quantum-mechanical and classical predictions. As the resonance plane was identified by means of the tilted detector, we assumed ideal longitudinal alignment in the analytical calculation. We emphasize that the model contains several simplifying assumptions and is, thus, only suitable for a qualitative comparison with the data.

The evidence described in this paper allows us to conclude that we successfully observed positron interference in the Talbot-Lau regime. Considering the six orders of magnitude difference between the typical transit time through the interferometer (10 ns) and the average time distance between two consecutive positrons (10 ms), a genuine single-particle experiment was realized. In this regime, any interaction between the interfering particles can be neglected. Echoing the "double-slit" electron experiments of Merli *et al.* (*10*) and Tonomura *et al.* (*34*), our measurement illustrates the principle of wave-particle duality: Positrons are emitted as point-like particles by a radioactive source, interact as de Broglie waves with the interferometer, and are eventually detected as distinct spots in the emulsion detector. Their spatial distribution is driven by λ_{dB} as predicted by quantum mechanics, providing the first demonstration of antimatter wave interferometry.

This result is the first step in the QUPLAS (QUantum interferometry with Positrons and LASers) program (*21*, *23*, *24*, *35*) and paves the way not only to interferometric studies on neutral antimatter systems such as positronium, muonium, or antihydrogen but also to the measurement of their gravitational acceleration in the field of Earth. The technique we demonstrated is able to cope with the poor coherence and low intensity of realistic antimatter beams. It thus represents a realistic option to tackle the search for violations of the weak equivalence principle with antimatter systems.

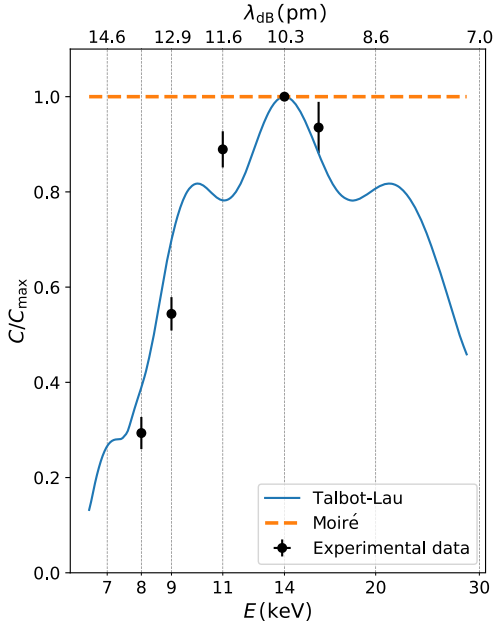

Fig. 5. Contrast as a function of energy. Measured contrast normalized to the resonance value, defined as $C/C_{max}(E)$. The 68% confidence interval uncertainties are obtained by standard error propagation. The solid line is the quantum-mechanical prediction, while the classical prediction is indicated by the dashed line.

MATERIALS AND METHODS

Modeling the positron beam

We made use of an analytical model describing grating interferometry with partially coherent beams (*25*). In addition to the de Broglie wavelength, it requires three input parameters given on an arbitrary initial plane: w_0 (beam width), l_0 (transverse coherence length), and r_0 (radius of wavefront curvature). The model assumes a Gaussian transverse beam intensity profile with FWHM = $2w_0\sqrt{\log 2/\pi}$ and provides analytical evolution equations for the three parameters along the optical axis (z). If the initial reference plane is the one where the beam size is at a minimum, then the equations for $w(z)$ and $l(z)$ reduce to

$$w(z) = w_0\sqrt{1+\left(\frac{z\lambda_{dB}}{w_0 l_0}\right)^2} \quad (4)$$

$$l(z) = l_0\sqrt{1+\left(\frac{z\lambda_{dB}}{w_0 l_0}\right)^2} \quad (5)$$

Since the beam was slit collimated, we used an analytical approximation (*36*) to determine w_0. By measuring the beam size at a known distance from the initial plane, the first equation can be solved for l_0. The beam size measurements were conducted by means of a moving absorbing target to mask the beam coupled to a BaF_2 gamma detector monitoring the transmitted rate (fig. S3). This system allowed us to determine the FWHM beam size at the emulsion detector plane with an accuracy of about 0.5 mm. Since a 0.1% change in energy from the resonance value only amounts to a relative contrast loss $\Delta C/C \sim 0.2\%$, the beam is treated as monochromatic. Electrostatic interactions with the grating bars are also negligible in the adopted setup as discussed in a previous publication (*35*). Furthermore, it is worth noting that treatment assumed infinitely extending and perfectly parallel gratings.

Rotational grating alignment

Rotational alignment took place on a dedicated optical table (fig. S4) and was based on the Fraunhofer diffraction of a 670-nm diode laser by the micrometric diffraction gratings. The setup is shown in fig. S5A: The first-order maxima produced by the first grating can propagate beyond the second grating, as they are diffracted at a ~34° angle. On the other hand, first-order maxima of the second grating are diffracted at a larger angle of ~42° due to the $d_1 > d_2$ condition. When the grating slits are perfectly parallel, a unique intersection of the two pairs of the first-order maxima exists. Two cameras were used to monitor the superposition of the two pairs of spots as the second grating was rotated by a piezoelectric rotator. Since the diffracted rays follow spatially separated paths toward the cameras, they could be masked one at a time to allow subpixel accuracy in the detection of the spot center. This was estimated by means of a Gaussian fit with a resulting uncertainty of about 2 μm. If one of the two gratings was tilted about the x axis, then the spots would have appeared on the plane of the cameras as shown

in fig. S5B. Under that condition, spot superposition on one side no longer corresponds to exact rotational alignment. For this reason, the first grating was positioned on a mirror mount to control its tilt with respect to the optical axis. Superposition of the two pairs of spots within <10 μm on both sides was ensured before each measurement. This corresponds to an angular alignment $\phi < 30$ μrad since the intersection points are located ~0.3 m away from the optical axis. Alignment was then checked after each measurement, and the condition $\phi < 70$ μrad held for all cases. We emphasize that the estimated tolerance to misalignment is $\sigma_\phi \sim 550$ μrad; therefore, $\phi = 70$ μrad would only introduce a relative contrast loss of 0.8%. Furthermore, part of the observed angular drift was likely the result of moving the interferometer from the alignment table to the vacuum chamber.

Positron transmission through the grating bars

The 700-nm-thick silicon nitride grating bars are gold plated with a ~10-nm-thick gold layer and transmit a sizeable fraction of positrons at 14 keV. By means of Monte Carlo simulations based on the PENELOPE software (*37*), we estimated the transmission probability from a grating bar to be (64.3 ± 0.3)%, (49.2 ± 0.3)%, (16.4 ± 0.3)%, (1.5 ± 0.5)%, and <0.1% for 16, 14, 11, 9, and 8 keV, respectively. A total of 50,000 positron trajectories were simulated for each energy. The angular distribution of the transmitted positrons with respect to an axis normal to the surface was for all energies well approximated by a Gaussian function with a standard deviation of about 0.6 rad. The PENELOPE package accounts for surface interactions at the membrane exit. Experimental results in the literature (*38*) indicate that a broad angular distribution is expected. Positrons transmitted by the grating bars would produce a Gaussian distribution of grains on the emulsion, superimposed to the interference signal, with FWHM ~0.8 m. On the other hand, the typical size of the beam spot was 6.5 mm FWHM. This energy-dependent contribution to background noise was thus suppressed by a factor 10^4 in terms of grain density with respect to thermal-induced background. For this reason, the effect had no measurable impact on the observed contrast modulation.

SUPPLEMENTARY MATERIALS

Supplementary material for this article is available at http://advances.sciencemag.org/cgi/content/full/5/5/eaav7610/DC1

Fig. S1. Picture of two emulsion detectors after exposure to the beam and chemical development.

Fig. S2. Optimal angle and period found via the Rayleigh test.

Fig. S3. Picture of the apparatus.

Fig. S4. Picture of the interferometer.

Fig. S5. Schematics of the rotational alignment procedure.

Movie S1. Animation based on actual data from the scanned emulsion film showing the buildup of the interference pattern.

REFERENCES AND NOTES

1. L. de Broglie, Waves and quanta. *Nature* **112**, 540 (1923).
2. L. de Broglie, Recherches sur la théorie des quanta. *Ann. Phys.* **3**, 22–128 (1925).
3. C. J. Davisson, L. H. Germer, Reflection of electrons by a crystal of nickel. *Proc. Natl. Acad. Sci. U.S.A.* **14**, 317–322 (1928).
4. G. P. Thomson, A. Reid, Diffraction of cathode rays by a thin film. *Nature* **119**, 890 (1927).
5. H. Rauch, W. Treimer, U. Bonse, Test of a single crystal neutron interferometer. *Phys. Lett. A* **47**, 369–371 (1974).
6. A. Zeilinger, R. Gähler, C. G. Shull, W. Treimer, W. Mampe, Single- and double-slit diffraction of neutrons. *Rev. Mod. Phys.* **60**, 1067–1073 (1988).
7. M. S. Chapman, C. R. Ekstrom, T. D. Hammond, R. A. Rubenstein, J. Schmiedmayer, S. Wehinger, D. E. Pritchard, Optics and interferometry with Na_2 molecules. *Phys. Rev. Lett.* **74**, 4783–4786 (1995).
8. M. Arndt, O. Nairz, J. Vos-Andreae, C. Keller, G. van der Zouw, A. Zeilinger, Wave–particle duality of C_{60} molecules. *Nature* **401**, 680–682 (1999).
9. B. Brezger, L. Hackermüller, S. Uttenthaler, J. Petschinka, M. Arndt, A. Zeilinger, Matter-wave interferometer for large molecules. *Phys. Rev. Lett.* **88**, 100404 (2002).
10. P. G. Merli, G. F. Missiroli, G. Pozzi, On the statistical aspect of electron interference phenomena. *Am. J. Phys.* **44**, 306–307 (1976).
11. I. J. Rosenberg, A. H. Weiss, K. F. Canter, Low-energy positron diffraction from a Cu(111) surface. *Phys. Rev. Lett.* **44**, 1139–1142 (1980).
12. J. F. Clauser, S. Li, Talbot-vonLau atom interferometry with cold slow potassium. *Phys. Rev. A* **49**, R2213–R2216 (1994).
13. K. Kirch, K. S. Khaw, Testing antimatter gravity with muonium. *Int. J. Mod. Phys. Conf. Ser.* **30**, 1460258 (2014).
14. D. B. Cassidy, S. D. Hogan, Atom control and gravity measurements using Rydberg positronium. *Int. J. Mod. Phys. Conf. Ser.* **30**, 1460259 (2014).
15. T. J. Philips, Antimatter gravity studies with interferometry. *Hyperfine Interact.* **109**, 357–365 (1997).
16. M. G. Giammarchi; AEGIS Collaboration, AEGIS at CERN: Measuring antihydrogen fall. *Few-Body Syst.* **54**, 779–782 (2013).
17. A. Kellerbauer, M. Amoretti, A. S. Belov, G. Bonomi, I. Boscolo, R. S. Brusa, M. Büchner, V. M. Byakov, L. Cabaret, C. Canali, C. Carraro, F. Castelli, S. Cialdi, M. de Combarieu, D. Comparat, G. Consolati, N. Djourelov, M. Doser, G. Drobychev, A. Dupasquier, G. Ferrari, P. Forget, L. Formaro, A. Gervasini, M. G. Giammarchi, S. N. Gninenko, G. Gribakin, S. D. Hogan, M. Jacquey, V. Lagomarsino, G. Manuzio, S. Mariazzi, V. A. Matveev, J. O. Meier, F. Merkt, P. Nedelec, M. K. Oberthaler, P. Pari, M. Prevedelli, F. Quasso, A. Rotondi, D. Sillou, S. V. Stepanov, H. H. Stroke, G. Testera, G. M. Tino, G. Trénec, A. Vairo, J. Vigué, H. Walters, U. Warring, S. Zavatarelli, D. S. Zvezhinskij; (AEGIS Proto-Collaboration), Proposed antimatter gravity measurement with an antihydrogen beam. *Nucl. Instrum. Methods Phys. Res. B* **266**, 351–356 (2008).
18. P. Pérez, D. Banerjee, F. Biraben, D. Brook-Roberge, M. Charlton, P. Cladé, P. Comini, P. Crivelli, O. Dalkarov, P. Debu, A. Douillet, G. Dufour, P. Dupré, S. Eriksson, P. Froelich, P. Grandemange, S. Guellati, R. Guérout, J. M. Heinrich, P.-A. Hervieux, L. Hilico, A. Husson, P. Indelicato, S. Jonsell, J.-P. Karr, K. Khabarova, N. Kolachevsky, N. Kuroda, A. Lambrecht, A. M. M. Leite, L. Liszkay, D. Lunney, N. Madsen, G. Manfredi, B. Mansoulié, Y. Matsuda, A. Mohri, T. Mortensen, Y. Nagashima, V. Nesvizhevsky, F. Nez, C. Regenfus, J.-M. Rey, J.-M. Reymond, S. Reynaud, A. Rubbia, Y. Sacquin, F. Schmidt-Kaler, N. Sillitoe, M. Staszczak, C. I. Szabo-Foster, H. Torii, B. Vallage, M. Valdes, D. P. Van der Werf, A. Voronin, J. Walz, S. Wolf, S. Wronka, Y. Yamazaki, The GBAR antimatter gravity experiment. *Hyperfine Interact.* **233**, 21–27 (2015).
19. P. Hamilton, A. Zhmoginov, F. Robicheaux, J. Fajans, J. S. Wurtele, H. Müller, Antimatter interferometry for gravity measurements. *Phys. Rev. Lett.* **112**, 121102 (2014).
20. D. B. Cassidy, Experimental progress in positronium laser physics. *Eur. Phys. J. D* **72**, 53 (2018).
21. S. Sala, M. Giammarchi, S. Olivares, Asymmetric Talbot-Lau interferometry for inertial sensing. *Phys. Rev. A* **94**, 033625 (2016).
22. P. J. Schultz, K. G. Lynn, Interaction of positron beams with surfaces, thin films, and interfaces. *Rev. Mod. Phys.* **60**, 701–779 (1988).
23. S. Aghion, A. Ariga, T. Ariga, M. Bollani, E. Dei Cas, A. Ereditato, C. Evans, R. Ferragut, M. Giammarchi, C. Pistillo, M. Romé, S. Sala, P. Scampoli, Detection of low energy antimatter with emulsions. *J. Instrum.* **11**, P06017 (2016).
24. S. Aghion, A. Ariga, M. Bollani, A. Ereditato, R. Ferragut, M. Giammarchi, M. Lodari, C. Pistillo, S. Sala, P. Scampoli, M. Vladymyrov, Nuclear emulsions for the detection of micrometric-scale fringe patterns: An application to positron interferometry. *J. Instrum.* **13**, P05013 (2018).
25. B. McMorran, A. D. Cronin, Model for partial coherence and wavefront curvature in grating interferometers. *Phys. Rev. A* **78**, 013601 (2008).
26. B. Brezger, M. Arndt, A. Zeilinger, Concepts for near-field interferometers with large molecules. *J. Opt. B: Quantum Semiclassical Opt.* **5**, S82–S89 (2003).
27. A. D. Cronin, B. McMorran, Electron interferometry with nanogratings. *Phys. Rev. A* **74**, 061602 (2006).
28. A. Ereditato, The study of neutrino oscillations with emulsion detectors. *Adv. High Energy Phys.* **2013**, 382172 (2013).
29. C. Amsler, A. Ariga, T. Ariga, S. Braccini, C. Canali, A. Ereditato, J. Kawada, M. Kimura, I. Kreslo, C. Pistillo, P. Scampoli, J. W. Storey, A new application of emulsions to measure the gravitational force on antihydrogen. *J. Instrum.* **8**, P02015 (2013).
30. A. Ariga, T. Ariga, Fast 4pi track reconstruction in nuclear emulsion detectors based on GPU technology. *J. Instrum.* **9**, P04002 (2014).
31. K. V. Mardia, *Statistics of Directional Data* (Academic Press, 1972).
32. S. Aghion, O. Ahlén, C. Amsler, A. Ariga, T. Ariga, A. S. Belov, K. Berggren, G. Bonomi, P. Bräunig, J. Bremer, R. S. Brusa, L. Cabaret, C. Canali, R. Caravita, F. Castelli, G. Cerchiari, S. Cialdi, D. Comparat, G. Consolati, H. Derking, S. Di Domizio, L. Di Noto, M. Doser, A. Dudarev, A. Ereditato, R. Ferragut, A. Fontana, P. Genova, M. Giammarchi, A. Gligorova, S. N. Gninenko, S. Haider, T. Huse, E. Jordan, L. V. Jørgensen, T. Kaltenbacher, J. Kawada, A. Kellerbauer, M. Kimura, A. Knecht, D. Krasnický, V. Lagomarsino, S. Lehner,

A. Magnani, C. Malbrunot, S. Mariazzi, V. A. Matveev, F. Moia, G. Nebbia, P. Nédélec, M. K. Oberthaler, N. Pacifico, V. Petràček, C. Pistillo, F. Prelz, M. Prevedelli, C. Regenfus, C. Riccardi, O. Røhne, A. Rotondi, H. Sandaker, P. Scampoli, J. Storey, M. A. Subieta Vasquez, M. Špaček, G. Testera, R. Vaccarone, E. Widmann, S. Zavatarelli, J. Zmeskal, A moiré deflectometer for antimatter. *Nat. Commun.* **5**, 4538 (2014).
33. M. K. Oberthaler, S. Bernet, E. M. Rasel, J. Schmiedmayer, A. Zeilinger, Inertial sensing with classical atomic beams. *Phys. Rev. A* **54**, 3165–3176 (1996).
34. A. Tonomura, J. Endo, T. Matsuda, T. Kawasaki, H. Ezawa, Demonstration of single electron buildup of an interference pattern. *Am. J. Phys.* **57**, 117–120 (1989).
35. S. Sala, F. Castelli, M. Giammarchi, S. Siccardi, S. Olivares, Matter-wave interferometry: Towards antimatter interferometers. *J. Phys. B: At., Mol. Opt. Phys.* **48**, 195002 (2015).
36. B. McMorran, A. Cronin, Gaussian schell source as model for slit-collimated atomic and molecular beams. arXiv:0804.1162 [physics.optics] (8 April 2008).
37. J. Baró, J. Sempau, J. M. Fernández-Varea, F. Salvat, PENELOPE: An algorithm for Monte Carlo simulation of the penetration and energy loss of electrons and positrons in matter. *Nucl. Instrum. Methods Phys. Res. B* **100**, 31–46 (1995).
38. D. A. Fischer, K. G. Lynn, D. W. Gidley, High-resolution angle-resolved positron reemission spectra from metal surfaces. *Phys. Rev. B.* **33**, 4479–4492 (1986).

Acknowledgments: We would like to thank S. Cialdi and M. Potenza for contributions to the laser alignment systems. We acknowledge the support received from S. Aghion, G. Maero, and M. Romè on beam operations. We are grateful to S. Olivares and F. Castelli for theoretical insights. We are in debt to T. Ariga for sharing expertise in emulsion production. We acknowledge M. Bollani and M. Lodari for useful discussions. We thank R. Haenni for efforts with machining work and M. Vladymyrov, who developed the data acquisition software. We thank T. Savas for the fabrication of the diffraction gratings. We also thank L. Miramonti, P. Lombardi, and G. Ranucci for providing useful equipment. **Funding:** Financial support from the Politecnico di Milano, the Istituto Nazionale di Fisica Nucleare, and the Laboratory for High Energy Physics of the University of Bern is acknowledged. **Author contributions:** R.F., M.G., C.P., and S.S conceived and conceptually designed the experiment. R.F., M.L., and S.S. performed the positron beam operations. R.F., M.L., and S.S. designed, implemented, and commissioned the interferometer. A.A., A.E., C.P., and P.S. were responsible for the emulsion detectors and for the scanning facility. C.P. and S.S. performed the data taking and data analysis. The manuscript was written by S.S. and then edited and improved by A.E., R.F., M.G., C.P., S.S., and P.S. This experiment is the subject of S.S.'s PhD thesis. **Competing interests:** The authors declare that they have no competing interests. **Data and materials availability:** All data needed to evaluate the conclusions in the paper are present in the paper and/or the Supplementary Materials. The raw data generated in this experiment are available from the corresponding author upon reasonable request.

Submitted 17 October 2018
Accepted 25 March 2019
Published 3 May 2019
10.1126/sciadv.aav7610

Citation: S. Sala, A. Ariga, A. Ereditato, R. Ferragut, M. Giammarchi, M. Leone, C. Pistillo, P. Scampoli, First demonstration of antimatter wave interferometry. *Sci. Adv.* **5**, eaav7610 (2019).

Science Advances

First demonstration of antimatter wave interferometry

S. Sala, A. Ariga, A. Ereditato, R. Ferragut, M. Giammarchi, M. Leone, C. Pistillo and P. Scampoli

Sci Adv **5** (5), eaav7610.
DOI: 10.1126/sciadv.aav7610